Removal of Nitrate from Water
Using TiO₂/ PVDF Membrane Photobioreactor

Sobhanipour, Ali Reza●

Chemical Injuries Research Center, Baqiyatallah University of Medical Sciences, Tehran, I.R. IRAN

*Khodabakhshi, Mohammad Reza**⁺

Applied Biotechnology Research Center, Baqiyatallah University of Medical Sciences, P.O. Box 1435915371
Tehran, I.R. IRAN

Karimian, Ramin

Chemical Injuries Research Center, Systems Biology and Poisonings Institute,
Baqyatallah University of Medical Sciences, Tehran, I.R. IRAN

Alizadeh, Mostafa

Applied Biotechnology Research Center, Baqiyatallah University of Medical Sciences, P.O. Box 1435915371
Tehran, I.R. IRAN

ABSTRACT: *Removing low-concentration nitrate from water is desirable because it may cause eutrophication when discharged, but it is challenging using current technologies. Membrane photobioreactor (MPBR) technology (which is the combination of membrane and microalgae cultivation) emerges as a suitable option to efficiently reduce the nutrient load from wastewater. This study developed a high-efficiency microalgal-bacterial Membrane PhotoBioReactor (MPBR) to biologically remove nitrate from water. In order to obtain low-fouling membranes, TiO₂ nanoparticles were entrapped in PVDF membranes prepared by the phase inversion method. Successful fabrication of composite membranes (PVDF/TNT) was confirmed by using XRD, FTIR, DSC, TGA, SEM, and AFM. Membrane properties were studied using contact angle, tensile strength, pure water flux, Bovine Serum Albumin (BSA) rejection, antifouling properties, and porosity. Compared with the pristine PVDF films, the hydrophilicity, permeability, and antifouling performance of the proposed membrane were improved. A laboratory-scale MBR equipped with a synthesized membrane was used to evaluate the performance of mixotrophic denitrification under different Carbon Nitrogen (C/N) ratios, Hydraulic Retention Times (HRT), Nitrate loading, and Influent alkalinity. Methanol was supplied as a carbon source. Almost complete denitrification was achieved when the bioreactor was fed with 75 mg/L $NO_3^- - N$, 150 mg/L methanol at 4 h HRT without external alkalinity supplementation. The results as a whole indicated that the MPBR can be applied effectively to the removal of nitrate from real wastewater.*

KEYWORDS: *Denitrification; Membrane photobioreactor; TiO₂/PVDF nanocomposite; Water treatment.*

INTRODUCTION

Excessive use of nitrogenous fertilizers in agricultural industry and inappropriate disposal of industrial and domestic wastewaters may lead to contamination of surface and ground waters. Nitrate can cause methemoglobinemia when ingested by infants, and could cause carcinoma, malformation and mutation when transformed into nitrosoamines[1]. In many countries, nitrate concentration in ground water has exceeded the maximum allowable limits for the drinking water. The United States Environmental Protection Agency set maximum contaminant levels of 10 mg NO_3–N/L and 1.0 mg NO_2–N/L for drinking water[2, 3]. Several physicochemical techniques are effective for the simultaneous removal of chromate and nitrate, including membrane filtration, reverse osmosis, electrodialysis, and ion exchange; however, the high cost of these approaches and the generated secondary wastes remain issues that need to be addressed [4, 5].

Although reverse osmosis, ion exchange, distillation and electrodialysis are effective physico/chemical methods for nitrate removal from water, high operational costs, low selectivity and the formation of secondary brine wastes are the main disadvantages[6, 7]. Physicochemical technologies and the combination of physicochemical and biological technologies (e.g. anaerobic-ozonation and aerobic-adsorption treatments) can effectively reduce the toxicity of wastewaters containing nitrates and heavy metals[8]. Nonetheless, their high chemical and energy requirements, prohibitive operating costs and generation of secondary pollution, which can jeopardize their economic and environmental sustainability, limit the full-scale implementation of physicochemical technologies[9, 10]. In contrast, biotechnologies have emerged as a cost-effective and environmental friendly alternative to physicochemical technologies for wastewater treatment, although biological processes are often limited by the low biodegradability of wastewater contaminants [11, 12]. Membrane BioReactors (MBR) function through a combination of biological remediation and membrane separation. These bioreactors offer the advantages of small footprint, high biomass retention, large loading rates, process flexibility and enhanced effluent quality [13, 14]. MBRs are typically associated with the activated sludge process, and these have commercial uses in the treatment of both municipal and industrial wastewater[15].

Among the different biological approaches proposed in recent years, the Microalgal Membrane PhotoBioReactor (MPBR) is a successful technique used in wastewater treatment [16, 17]; for this purpose, microalgae should be employed in large amounts for a long interval. Important critical limitation of microalgae use throughout treatment approaches is to recover and separate microalgae from effluent streams [18]. Immobilization of microalgae in MPBR, commonly called Hybrid Microalgae Membrane PhotoBioReactor process (HMPBR) or attached growth MPBR, is the solution introduced for this problem [19]. HMPBR is one of the biological Attached growth method which have more benefits than suspended growth methods, including more system stability during operation, higher resistance to changes in pH, temperature, toxic shocks, higher rate of substrate removal, capability to maintain biomasses in higher concentrations in shorter Hydraulic Retention Time (HRT), and washout prevailing [6, 20].

Many studies have achieved an excellent performance for bioreactor for nutrients removal efficiency. Microalgae can be cultured in various systems, from open ponds to closed PhotoBioReactors (PBR). Open ponds are cheap and easy to scale up, whereas PBR technologies offer greater potential in terms of productivity, control of culture conditions and applicability to cultivate various strains. The risk of contamination, the influence of existing environmental conditions (daylight, seasonal temperature, etc.) and to further increase biomass concentration seem to be more advantageous in many cases the use of photobioreactors. To the best of author's knowledge, simultaneous membrane and photobiorector has never been reported for nitrate removal. Therefore, the aim of this study is to propose a novel submerged mixotrophic membrane in a photobioreactor to investigate the removal of nitrate from aquatic environments. To do so, TiO_2 modified PVDF membrane was synthesisezd and characterized. TiO_2 was selected because of its remarkable photocatalytic activity, surface area and mesoporous volume [21]. Some species of microalgae are mixotrophic, meaning that they can simultaneously act through autotrophism and heterotrophism, consuming both the inorganic carbon (CO_2) and organic carbon contained in the substrate. The removal efficiency of nitrate under different Carbon and Nitrate ratios (C/Ns) and hydraulic retention times (HRTs) was investigated. A combination of various fibers was used as biofilm carriers; it can attach

algal cells and form a biofilm within the systems. The novel MPBR demonstrated a potential approach for nitrate removal and microalgae cultivation.

EXPERIMENTAL SECITON

Preparation of TiO₂ nanorods

All chemical reagents used in the present experiments were obtained from commercial sources and used without further purification. The TiO₂ nanorods are synthesized on FTO substrates through hydrothermal method without TiO₂ seed layer. 8 ml of concentrated hydrochloric acid (36.5%–38% by weight) was mixed with 0.2 mL of titanium butoxide and the solution was stirred together with an amount of deionized water. The conductive side of the FTO substrate was placed face down in the precursor solution and then was placed in an oven at 150 °C for 150 min. After cooling down to room temperature and washed with deionized water, the TiO₂ nanorod arrays were obtained. Then it was annealed in the air atmosphere at 350 °C for 2 h, to yield better crystallization.

The morphology of the nanorods was observed by scanning electron microscopy (FE-SEM, S-4700, Hitachi, Japan) and their crystal structure was studied by an X-ray diffractometer (Smart Lab; Rigaku). The microstructure of nanowires were investigated by Transmission Electron Microscopy (TEM; Tecnai Model F20; FEI). The X-Ray Diffraction (XRD) spectrum was recorded by the Bruker D8 X-ray diffractometer. Selected Area Electron Diffraction (SAED) pattern was performed by using TECNAI F20 Philips, operating at an acceleration voltage 200 kV. The valence states of elements deposited on sample surface was studied by X-ray photoelectron spectroscopy (XPS; VG Multilab 2000, Thermo VG Scientific, UK).

Preparation of the membrane

TiO₂ was modified by incorporating polyethylene glycol (PEG) 2000 before fabricating the membrane. PEG usually served as a pore-forming additive in PVDF preparation. The PEG grafted onto the surface of TiO₂ nanorods would increase the polarity of the nanoparticles and the resulting hybrid membranes, but also act as a pore-forming additive, thereby further increasing the flux and anti-fouling performance of the PVDF hybrid membrane.

As-prepared TiO₂ (0.5 g), PEG2000 (10 g), and ethanol (250 mL) were added in a 500 mL triflask. After stirring at 30 °C for 30 min, 0.25 g of concentrated hydrochloric acid (37%) was added to the triflask. The temperature was increased to 70 °C, and the mixture was stirred for 3 h. The products were obtained through several cycles of centrifugation–redispersion–washing and then dried in a vacuum drying oven at 60 °C.

TiO₂ content in fabricated PVDF membrane was 1.0 wt%, which is optimal for the stability and homogeneous distribution in the polymer matrix. The membrane was prepared using phase inversion method induced by immersion precipitation. TiO₂ nanorods was dispersed into 16.8 g N,N-dimethylacetamide (DMAC, Sigma Aldrich) and sonicated for 30 min for good dispersion. After dispersing the nanoparticles in the solvent, 0.4 g PVP (Mw ~ 534 kDa, Sigma-Aldrich) and 2.8 g PVDF polymer (MW ~ 10 kDa, Sigma-Aldrich) were added to the dope solution using continuous stirring for 24 h at around 25 °C. The PVP additive is soluble both in DMAc and H₂O, and is leached out of the solution during the phase inversion process. The resulted polymer/nanofiller solution was again sonicated for 10 min to remove air bubbles. Afterwards, the prepared solution was casted on the smooth glass plates using a film applicator (Elcometer 3530, UK) with the same thickness of 150 μm. The prepared film was quickly immersed in a coagulation bath (distilled water as non-solvent) at the room temperature without evaporation. After primary phase separation, the prepared membrane was stored in distilled water for 24 h in order to completion of the phase separation. Finally, the prepared membrane was placed between two sheets of filter papers for 24 h at room temperature for drying.

Membrane surface and its cross-section morphology were analyzed using a SEM and AFM (Nanosurf® Mobile S scanning probe-optical microscope, Switzerland). For the cross section measurement, membranes were fractured in a cryogenic condition using liquid nitrogen. The surface hydrophilicity of both pure and blended membranes were evaluated by water contact angle measurement. The water droplet (1.0 μL) permeation process was recorded using speed optimum video measuring unit equipped with Dataphysics OCA20, Germany. The measurements were controlled at 298 K. The membrane porosity was calculated on the basis of its dry–wet weight[13]. FT-IR analysis was performed on a Perkin Elmer Spectrum 2000 spectrometer with a resolution of 1 cm⁻¹. The surfaces and cross sections of the membranes were examined by a field-

Emission scanning electron microscope (FE-SEM, S-4700, Hitachi, Japan) at 5 kV acceleration voltage. Membranes were coated with platinum by ion sputtering (E-1030, Hitachi, Japan) before analysis. The cross-sections of membranes were prepared by cryofracture in liquid nitrogen. One hundred points from ten different SEM images of each membrane were analyzed to determine the thickness of the membranes, pore size and their size distribution. Thermal gravimetric analysis (TGA/DT) was performed to examine the thermal stability of synthesized materials by using TGA 8000 Perkin-Elmer, USA with a heating rate of 10 °C/min and differential scanning calorimetry (DSC) was done by means of Mettler Toledo 823e. Tensile strength of membranes was measured using testometric material testing machine, where strain rate was maintained at 2 mm/min.

The permeation properties of the membranes were tested using dead end filtration cell. An effective membrane area of 5 cm2 was used for permeation studies. The membranes were initially dipped in distilled water for 24 h before the filtration experiments. The membranes were compacted at 0.4 MPa transmembrane pressures (TMP) for 30 min. Then the pressure was reduced to 0.2 MPa, TMP and time dependent pure water flux of the different membranes was measured for every 1 min time interval. The pure water flux (PWF) of the membranes was calculated using the following equation:

$$J_{w1} = \frac{V}{A \times t} \tag{1}$$

Where J_{w1} is the pure water flux (L/m^2 h), V is the permeate volume (L), A is the membrane area (m^2) and t is the time (h).

The antifouling property of the membranes was determined using reported procedure in literature [30]. In brief, the pure water flux of the membrane was determined J_{w1} (L/m^{2}h) at 0.2 MPa TMP. Bovine serum albumin (BSA) was considered as a model protein to study the antifouling property of the membranes. The aqueous solution of BSA with a concentration of 0.8 g/L was prepared and the solution was filtered through the membrane for 80 min. Then membrane was flushed with pure water for 15 min and pure water flux J_{w2} (L/m^{2}h) was measured again. Finally the membrane antifouling property was determined by calculating Flux Recovery Ratio (FRR) using the following equation:

$$FRR = \frac{J_{w2}}{J_{w1}} \times 100 \tag{2}$$

Photobioreactors preparation and start-up

A plexiglas MPBR (Fig. 1) was used in the study. The total and working volume of reactor respectively was 9.5 and 5 L. To attach pollutants to microalgae, solid carriers were placed into the MPBR; the media constitute 60% of total volume of MPBR reactor. The carrier provided by Aramis green environmental protection technology co., Ltd. is composed of cotton, vinylon, polyvinylidene chloride and polypropylene fiber. The characteristics of the spiral fiber based biofilm reactor are strong adhesion of microorganisms, low cost and easy management. The employed fibers were 3×0.5 cm with 0.17 carrier/g weight and tied to be bowknot. Prepared membrane as a solid–liquid separator was immersed into reactors. PVDF based prepared membrane was used. During the experiment, the liquid level in the reactor was controlled by the upper and lower water level sensors (Depka, USA), which controlled the effluent pump (Watson-Marlow, Singapore, ±0.1L) to operate in an intermittent mode. Two gas distributors were installed at the bottom of the reactor. Air was pumped (Thomas Scientific, USA) into the reactor through one of the distributors at an aeration rate of 0.5 L/ min to form bubbles, which provided agitation in the column; no other mixing was used. Membrane permeate, 12 min On/12 min Off, is suctioned by a suction pump (Thomas Scientific, USA). The lighting was provided by 5 red/blue LED lamps with a ratio of 1/4, with a power of 9 w. These lamps were located on top and side walls (at a distance of 5 cm from the surface) of the photobioreactor and they were used throughout the day for 12 h. For the entire duration of the experiments, the maximum light intensity on the surface of the reactor was about 8000 ± 9.7 lx, which was measured at the surface of the mixed liquid within the photobioreactor. A peristaltic pump (PD5201, Heidolph, Germany) was used to inject the influent flow into the system. While using the maximum level of membrane flow, the transmembrane pressure was monitored consecutively (Troshcer, Germany); if TMP exceeds the maximum permissible levels (30 kpa), the membrane module is washed with distilled water for 30 min outside the system and then, was placed into the photobioreactor. All the instruments used in the system, including hoses and dishes were in black

or dark-brown colors, or covered with foil sheets, in addition all the dishes were sterilized using autoclave to prevent the growth of microalgea outside of the photobioreactors. To excrete the sludges may accumulated in the reservoir, a drain valve was embedded into the bioreactor bottom. The photobioreactor was started up first by biological adaptation and microalgea acclimazation. Filtration pressure, pH and ORP (Hanna, USA) were recorded online via a computerized system.

The reactor was seeded with denitrifying bacteria obtained from a sulfur-packed column bioreactor and operated at an infinite sludge age with no sludge wastage. The influent wastewater was homogenous; however, to make a circulation in the wastewater flow from bottom to the surface of reservoir per 15 min and maintain wastewater quality an immersed pump was used. To excrete the sludges may accumulated in the reservoir, a drain valve was embedded into the bioreactor bottom. The schematic of reactor has been presented in Fig. 1.

Photobioreactor operation procedure

The reactor was fed with tap water supplemented with 50 mg/L K_2HPO_4 as a source of phosphorus, and different concentrations of KNO_3 to obtain the predetermined nitrate concentrations (Table 1). Additionally, the feed water was supplemented with 750 mg/L[1] $NaHCO_3$ (equal to 446 mg/L $CaCO_3$) in periods 1–7 to neutralize the acid generated during autotrophic denitrification process (Table 1). After stimulation of simultaneous heterotrophic and autotrophic denitrification process by methanol supplementation, $NaHCO_3$ concentration was decreased step by step and eliminated completely in the last operational stage. During the study of mixotrophic process, methanol was supplemented as an external organic carbon at 28 mg/L or 56 mg/L Dissolved Organic Carbon (DOC) concentrations (Table 1).

Analytical methods

The photobioreactors results were obtained under constant conditions. The bioreactors in each phase worked until obtaining the steady-state condition that was repeated 3–5 times. Steady-state condition can be obtained if removal efficiency SD is <5%. A DO meter (MI-65; Martini Instruments) was used to measure DO and the pH meter to measure pH (HACH; Germany). Nitrate

1. Reservoir of feedstock
2. Electric heater
3. Electric mixer
4. Peristaltic pump
5. MPBR reactor
6. Submerged membrane
7. Diffuser
8. pH meter
9. Discharge sludge port
10. Solid biofilm carrier
11. Gauge
12. Suction pomp
13. Reservoir of outlet
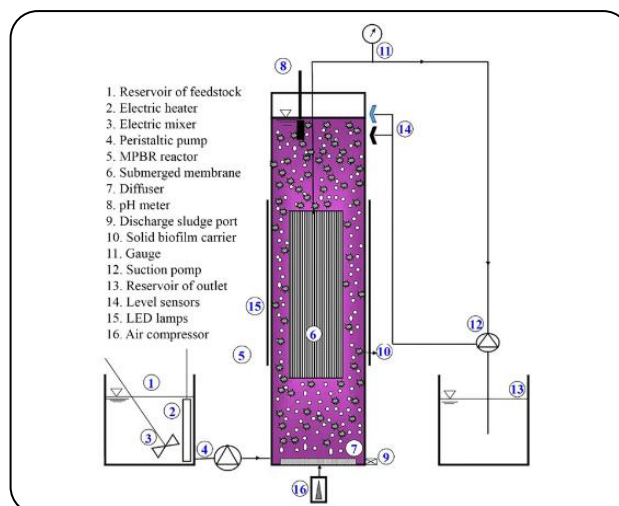14. Level sensors
15. LED lamps
16. Air compressor

Fig. 1: Schematics of MPBR photobioreactor.

was measured using Ion Chromatography (HPLC) (IC 5000, DIONEX). The concentration of microalgae biomass suspended in the system was measured based on Optical Density (OD) in a mixed solution at 540 nm using a UV/Vis spectrophotometer and then, the biomass concentration was determined as: dry cell weight (mg/L) = $542 \times OD_{540}$. Determining the biomass amount attached to the biofilm carriers, 30 carriers -representing 0.5% of the total carriers- were collected from MPBR and dried at 105 °C for 2 h. The dry carriers were weighed and to determine the biomass weight attached to the carriers, the original weight of carriers was subtracted from the obtained weight. The attached biomass concentration was then expressed as mg/L based on the carriers total number and the reactor working volume [22]. The data were calculations in triplicate.

RESULTS AND DISCUSSION
Characterization of nanocomposite

Fig. 2 shows the typical SEM and TEM images of the nanorod arrays. As shown in Fig. 2a & b, the entire surface of the FTO substrate is uniformly covered with TiO_2 cuboid nanorods. The inserted image is the cross-sectional view of the sample, clearly showing that the TiO_2 cuboid nanorods are nearly perpendicular to the FTO substrate and the length and diameter of them are about 3.5 μm and 68nm, respectively. In order to further explore the morphologies of the samples, the nanorods were scraped from FTO substrates and studied by TEM analysis, respectively, which are shown in Fig. 2c.

Table 1: Operational conditions of the column reactors.

Periods	1	2	3	4	5	6	7	8	9	10
Days	0–35	35–53	53–65	65–75	75–91	91–111	111–138	138–157	157–178	178–200
NO_3–N (mg/L)	50	50	50	50	75	75	75	75	75	75
HRT (h)	10.5	7.27	6.0	4.0	4.0	4.0	4.0	4.0	4.0	4.0
Loading (mg NO_3–N/Ld)	110	170	200	300	450	450	450	450	450	450
Influent alkalinity (mg/L $CaCO_3$)	575	575	575	575	575	575	575	337	237	140
Methanol (mg/L)	–	–	–	–	–	75	150	150	150	150
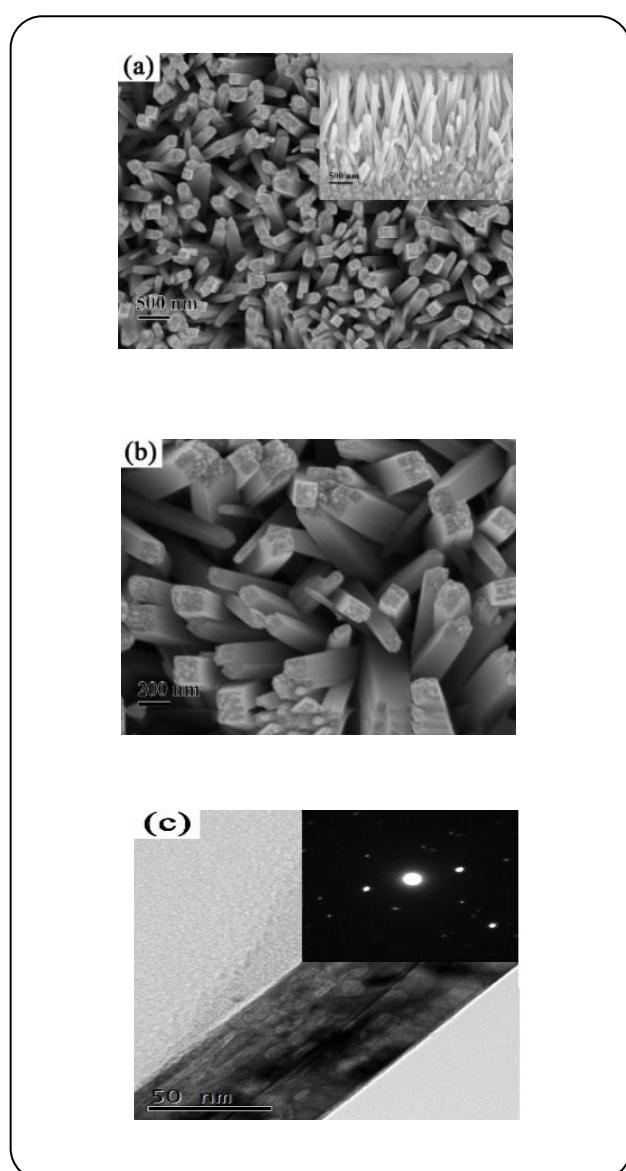
Fig. 2: SEM (a, b) and TEM (c) images of TiO₂ nanorods.

From the TEM image and corresponding SAED pattern of one TiO_2 nanorod, it can be seen that the nanorod is rutile structure and single crystalline[23]. There is no other phase coating over the surface of the nanorod.

Fig. 3 is an XRD pattern of TiO_2 film grown on a FTO. The diffraction reflections at $2\theta = 36.22°$, $41.41°$, $54.51°$, 62.93 and 69.97 in the pattern correspond to the (1 0 1), (1 1 1), (2 2 0), (0 0 2) and (1 1 2) crystal planes of the rutile TiO_2 crystal, respectively, and the results are compared with the standard XRD pattern (JCPDS 65-192 #). The remaining diffraction reflections originate from the FTO substrate (JCPDS 77-452 #) [24]. This XRD pattern shows that the diffraction intensity of the (0 0 2) crystal plane is the highest in all TiO_2 crystal diffraction reflections. This indicates that the TiO_2 crystals do crystallize along the normal direction of the specific crystal plane, which is also the most important factor for the formation of TiO_2 nanorods. No other impurity peak in XRD pattern indicating no traces of secondary phases such as anatase or brookite were observed. The presence of broad XRD peaks is an indication of small crystallite size in the range of nanoscale, affirming the nanocrystalline nature of the TiO_2 samples. The rutile phase of TiO_2 is tetragonal and exhibits symmetry characters of the space group with two TiO_2 molecules per unit cell[19]. Average crystallite size of TiO_2 samples were calculated by using Scherrer's formula. The calculated crystallite size of TiO_2 for (110) planes was 16.13 nm. SAED patterns of an individual nanorod of the rutile TiO_2 nanorods is shown in Fig. 4. The SAED image confirm that the TiO_2 nanorods synthesized directly on FTO glass are single-crystalline.

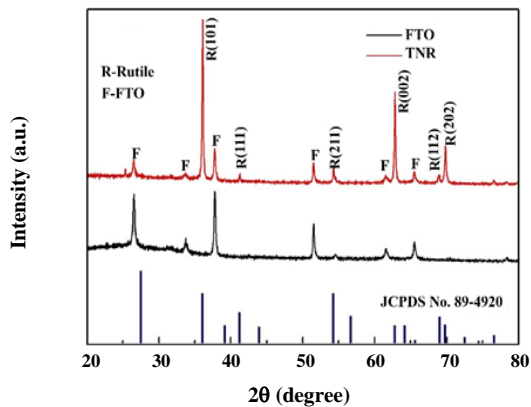The XPS analysis of TiO_2 thin films was performed to identify the composition and valence state of elements.

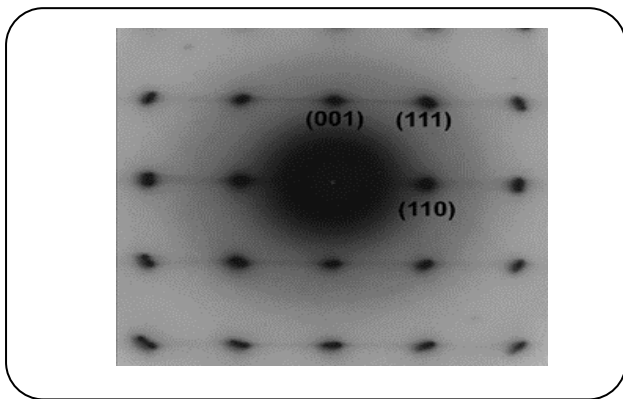**Fig. 3: X-ray diffraction patterns of the bare FTO and TiO₂ NRs.**

Fig. 4: SAED image of an individual nanorod of the single-crystal rutile TNRs.

The survey spectrum of nanorods is presented in Fig. 5a which shows presence of Ti, O and a small amount of adventitious carbon. The carbon peak is attributed to the residual carbon from XPS instrument itself. The peak at binding energy 284.87 eV corresponds to amorphous carbon. Ti 2p spectrum is shown in Fig. 5b consists of the distinct Ti 2p1/2 and Ti 2p3/2 signals that are located at 464.4 and 458.6 eV respectively[25]. The spin orbital splitting between these peaks is 5.8 eV which is comparable with that of 5.74 eV reported values, indicates Ti^{4+} oxidation state of titanium in TiO₂. Both Ti 2p signals are highly symmetric, and no shoulders were observed on the lower energy sides of Ti 2p3/2 signal, which indicate that the rutile TiO₂ nanocrystals are stoichiometric and the concentration of lattice defects is extremely low. The core level spectrum of oxygen is shown in Fig. 5c divided into two peaks at binding energy 529.98 and 531.21 eV[26]. The peak located at 529.98 eV attributed to oxygen

originating from lattice oxygen while peak at 531.21 eV suggesting the presence of surface hydroxyl groups[24]. Thus XPS spectrum confirms the Ti and O species in TiO₂ thin film with rutile phase.

Morphology and structure of the membrane

Fig. 6 shows the SEM images of the top surface of nanocomposite PVDF together with their respective cross sectional morphology. The morphological structure of PVDF membrane has greatly altered when the TiO₂ nanorods have been embedded by applying phase inversion technique. the prepared PVDF/ TiO₂ nanocomposite membrane exhibited porous-like structure, which indicated that there is excellent intersection connectivity between TiO₂ nanofiber and PVDF membrane matrix from top to the bottom of the cross-sectional morphology. It has been postulated that the membrane's internal structure plays an important role in determining the membrane performance [27]. The porous structure and uniformly distributed catalysts into the membrane are beneficial in the adsorption of pollutants within the entire membrane in the enhancement of the photodegradation[19] [27].The presence of nodules on the top surface of PVDF nanocomposite membrane could indicate the successful embedment of nanofillers throughout the substrate structure. From the cross section images, nanocomposite membranes showed long finger-like voids extended from the top to the bottom, while pristine PVDF showed short finger-like structure supported by macrovoid sublayer [28]. The introduction of TiO₂ nanofiller further enhanced the thermodynamic instability of the casting solutions. In the meantime, the hydrophilic groups of TiO₂ helped accelerate the exchange between solvent and nonsolvent [29]. Consequently, nanocomposite membrane showed the larger pore sizes than the corresponding pure PVDF membrane.

Fig. 7 presents three-dimensional AFM surface images of membranes PVDF and TiO₂/PVDF at a scan size of 10 μm × 10 μm. Evidently, the roughness of the membrane surface was affected by the introduction of nanomaterials into the polymer matrix. The surface roughness parameters, including average roughness (R_a), root-mean-square of the Z data (R_q), and height difference between the highest peak and the lowest valley (R_z), are shown in Table 2. It was clear that the roughness parameters of the hybrid membrane increased, indicating a smoother surface
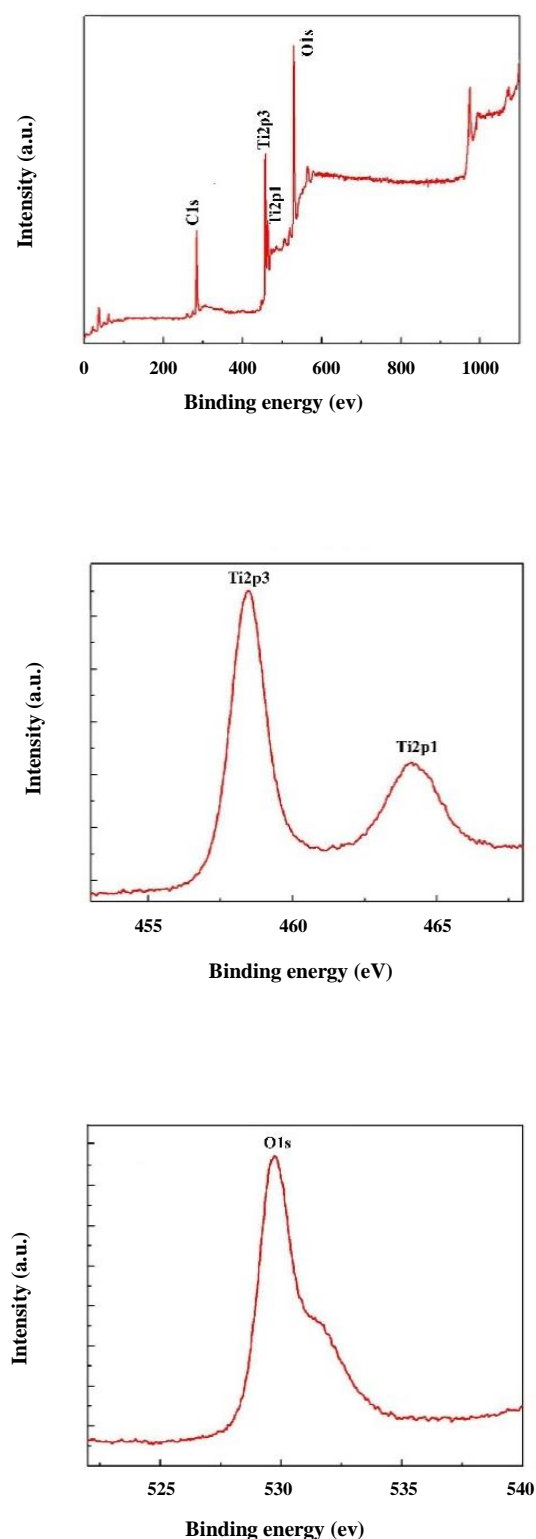
Fig. 5: (a) Experimental survey spectrum of TiO₂ ; (b) Core level spectrum of Ti2p and; (c) Core level spectrum of O1s of TiO₂ NRs.

relative for pure PVDF membrane. Therefore, the hybrid membranes presented antifouling properties better than those of the unmodified membrane.

The FTIR spectra of PVDF/TiO_2 hybrid membrane as well as the pure PVDF membrane were shown in Fig. 8. The FTIR studies had been carried out to ascertain the crystal phase of PVDF and the relationship between the polymer molecule and the nanoparticles. It could be seen from Fig. 8 that the curves of PVDF and PVDF/ TiO_2 superposed well at the higher wavenumber and deviated at the lower wavenumber. The deviation was ascribed to the addition of TiO_2. The band at 513 cm^{-1} was assigned to bending vibrations of CF_2 group [18]. The absorption bonds at 3027 and 2985 cm^{-1} were assigned to the nonsymmetrical and symmetrical stretching vibration of CH_2 groups [29]. The absorption peak at 1180 cm^{-1} was assigned to the stretching vibration of CF_2 groups. The deformed vibration of CH_2groups appeared at the frequency of 1400 cm^{-1} [30]. The peaks at 610, 760, 797, 976 cm^{-1} could be assigned to the typical peaks of α-phase PVDF crystals [28].

The contact angle can be interpreted as the measurement of the hydrophilicity of composite membranes, namely a composite membrane with a lower water contact angle exhibits a better hydrophilic property. The contact angles between water droplet and membranes were tested. It can be observed from Fig. 9 that the contact angle of PVDF/TiO_2 membranes is the lower (60.8°), which indicates that the hydrophilicity of PVDF/TiO_2composite membranes is better than pure PVDF membrane. This is because that TiO_2 can form hydrophilic surroundings on the surface of PVDF membranes; more hydroxide radicals are supplied by Ti–OH and a lot of Lewis acid sites, ensuring the formation of many hydrogen bonds between aqueous solution and PVDF [30]. Therefore PVDF/TiO_2 composite membrane shows higher hydrophilic property.

The surface pore radius and porosity of the membranes are presented in Table 3. The addition of TiO_2 to the membrane increases the pore size of it. The higher hydrophilicity of TiO_2 nanorods would cause an increase of pore size[31]. The porosity measurements indicate that the nanocomposite membranes have higher porosity than the pristine membrane. Thus the addition of TiO_2 has led to the increase in porosity of membranes which is evident from SEM images.
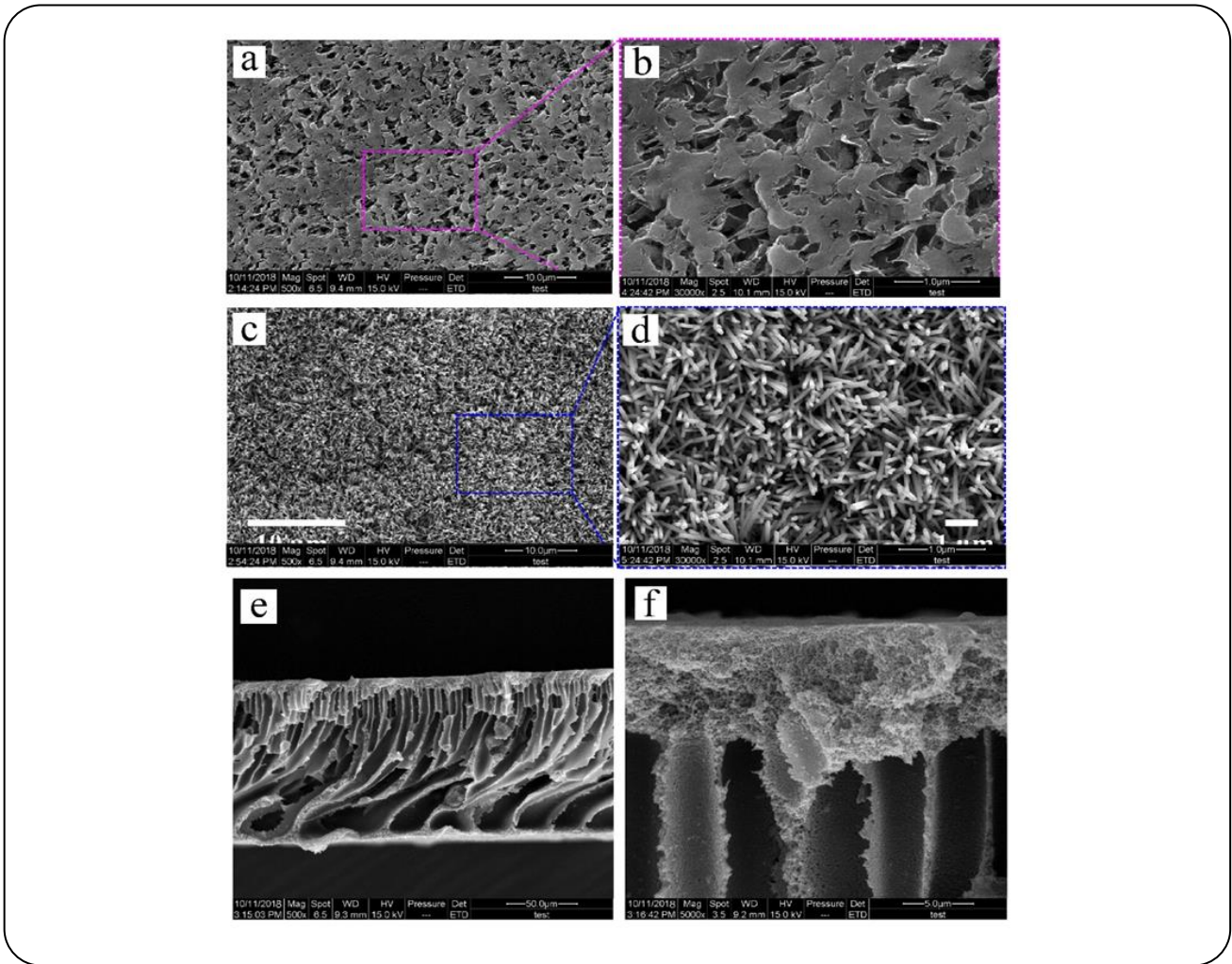
Fig. 6. SEM surface images of top and cross section of (a,b,e) PVDF membrane, (b) and (c,d,f) TiO2/PVDF membrane.
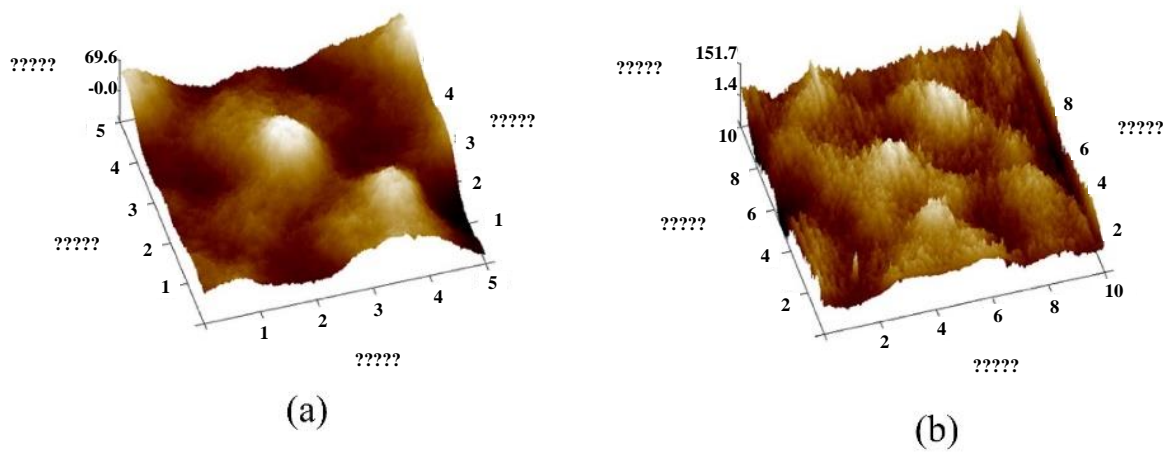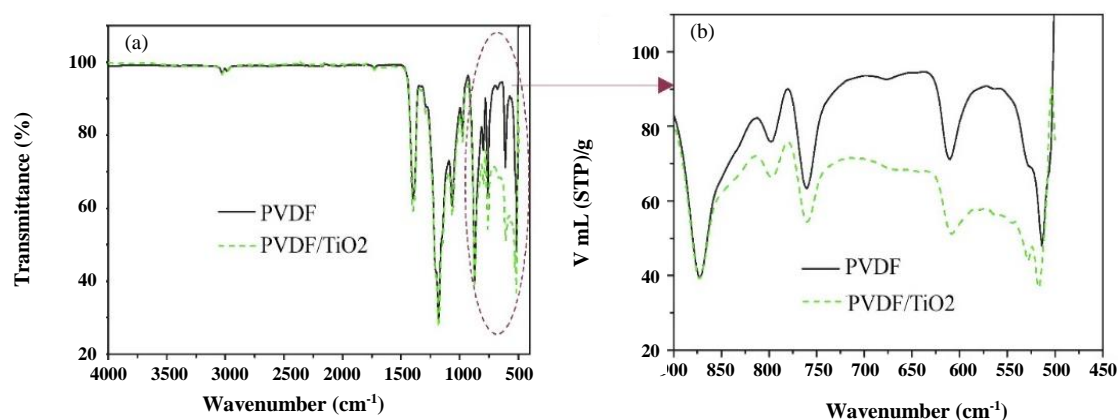

Fig. 7: AFM images of (a) PVDF (b) TiO2/PVDF membranes.

Table 2: Surface roughness parameters of the membranes.

Membranes	Roughness parameters		
	Ra	Rq	Rz
PVDF	16.7	21.4	139
TiO2/PVDF	31.9	40.6	355

Table 3: Mean pore radii and porosity of membranes.

| Membranes	Mean pore radius (nm)	Porosity (%)
PVDF	7.02	53.36
PVDF/TiO$_2$	10.86	76.09

Fig. 8: FTIR spectra of PVDF membrane and PVDF/TiO$_2$ hybrid membrane.
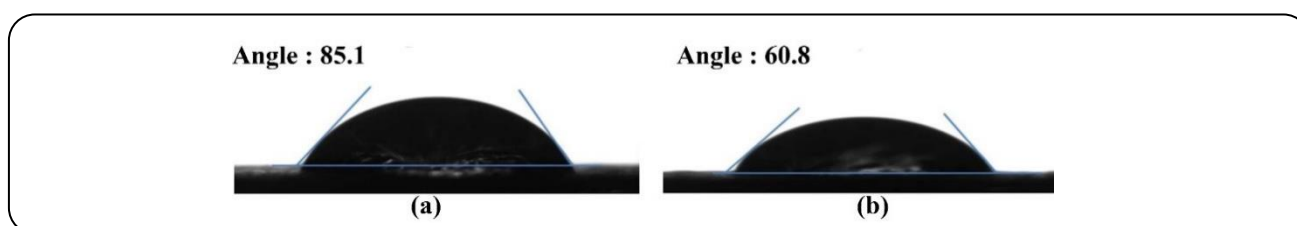
Fig. 9: Contact angles of a: PVDF b: PVDF/TiO$_2$.

The tensile properties, i.e. elongation at break and young moduli for membranes are calculated and tabulated in Table 4. It has been observed that by adding TNTs (as a filler), tensile strength of membrane enhanced. In comparison with initial value of the young's modulus, a 25% increase was observed and no prominent change in elongation at break value was observed. The TNTs dispersed around the PVDF membrane homogeneously which makes the distribution of pores uniform in the membrane.

Enhanced thermal stability is important criteria for composite membranes to be elaborated before applying these membranes for different applications. The TGA curves for neat and composite membranes were carried out and are shown in Fig. 10a, which indicate that the thermal stability of membranes increases with the addition of TNTs amount. The reason for this increase in stability is due to the enhancement of interactions between PVDF and TNTs. The degradation temperature was shifted from 393

Table 4: Tensile properties of PVDF/TNT membranes.

Membrane code	Young's modulus (MPa)	Tensile strength (MPa)	Elongation at break (%)
PVDF	80.30	03.01	33
PVDF/TiO₂	100.21	09.05	61
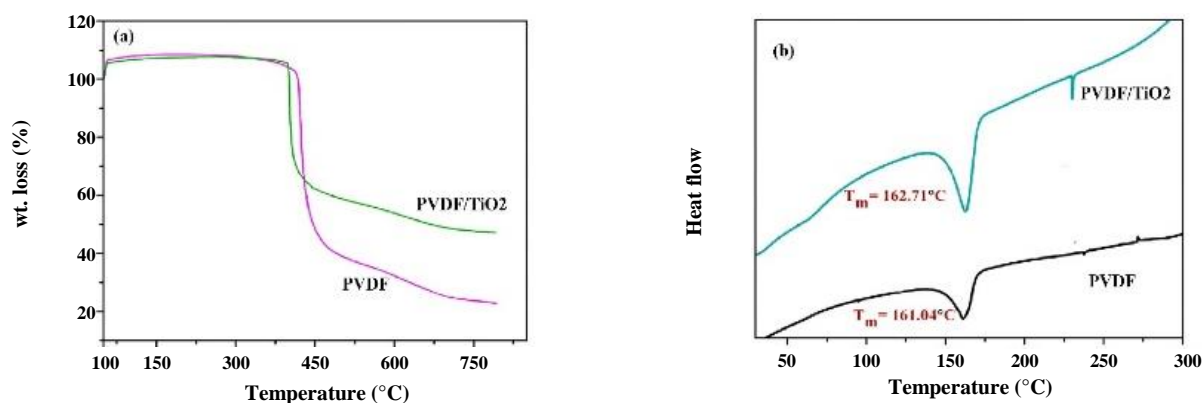
Fig. 10: (a) TGA curves for composite membranes and (b) DSC curves for composite membranes.

to 414 °C for PVDF/TiO$_2$. Glass transition temperature (T_g) and melting temperature (T_m) are other important characteristics which should be studied for composite membrane. DSC analysis was performed to find the T_g and T_m and the results are given in Fig. 10b. T_g was shifted from lower to higher value. The melting point for neat PVDF membrane is 161.04 °C. However, with the addition of TiO$_2$ a slight increase was recorded as 162.71 °C for PVDF/TiO$_2$. In general, TiO$_2$ have good thermal properties which limit the PVDF matrix decomposition and increase the thermal decomposition temperature of hybrid membranes [29].

Permeation properties of the membranes were studied by permeating pure water through the membranes using dead end filtration cell at 0.2 MPa, TMP. The pure water flux of the membranes is shown in Fig. 11. The nanocomposite membrane showed higher permeate flux than the pure membrane. Initially gradual decrease in pure water flux was observed for all the membranes during membrane compaction due to mechanical deformation of polymeric membrane matrix. The PVDF/TiO$_2$ nanocomposite membrane possessed higher hydrophilicity, higher porosity and better vertically interconnected pores than the PVDF membrane which led

to the water permeability of the membrane [32]. The stronger hydrophilic surroundings inside PVDF/TiO$_2$ channels and surface of membranes lead to form a water layer on the membrane surface [30] and more hydroxide radicals can interact with water molecule by hydrogen bonds, which makes water molecule pass through pore channel smoothly while most of oil droplets and suspend solids are intercepted by the membranes.

Fouling is due to hydrophobic interaction between foulant and membrane surface is the major drawback of membrane. Declined flux and shortening of membrane life time are the main outcomes of fouling. From Fig. 11, the flux decline behavior of the membranes was same during BSA rejection. Whereas pure PVDF membrane showed greater flux decline compared to PVDF/TiO$_2$ membrane. Since fouling study of the membranes assessed under similar hydrodynamic conditions, the difference in fouling behavior was due to TiO$_2$ presence in the membrane. Since the nanocomposite membranes had higher hydrophilicity, BSA molecules could not be easily adsorbed on the membrane surface indicating antifouling nature of membranes[23]. The figure shows decline in flux of membranes for initial few minutes. This initial decline of flux is due to the adsorption of BSA molecules onto
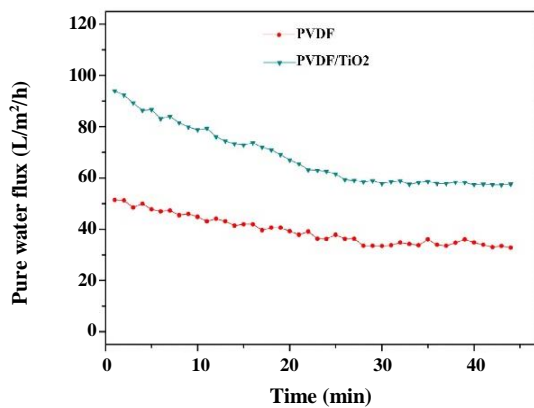
Fig. 10: Time dependent pure water flux of membranes at 0.2 MPa TMP and 26 °C.

Fig. 11: Flux of the membranes during BSA filtration.

the surface of the membranes [20]. The fouling resistance ratio (FRR) is the measure of antifouling property of the membranes. TiO₂NT incorporated membrane showed higher FRR values (83.25%) compared to pure PVDF membrane (65.61%). Higher the FRR value better is the antifouling nature of the membranes.

Nitrate removal in MPBR

Decreasing the HRT from 10.5 h to 4.0 h at influent nitrate concentration of 50 mg/L NO_3–N did not adversely affect the denitrification performance (Fig. 12). In the first four periods, the effluent nitrate and nitrite concentrations averaged 0.48 ± 0.82 mg L^{-1} NO_3–N and 0.12 ± 0.31 mg/L NO_2–N, respectively. Samples were also collected regularly from middle of the reactor. Although both NO_3–N and NO_2–N concentrations in the middle of the reactor were <1 mg/L when HRT was 6 h or higher (period 1–3), the concentrations averaged 1.1 ± 1.5 mg/L and 9.2 ± 4.3 mg/L, respectively, when the HRT was decreased to 4 h in the period 4 (data not shown). The laboratory test results about HRT showed an incremental effect, and the reason can be attributed to elevated contact of organic molecules with microorganisms. Between periods 1–4, the influent and effluent sulfate concentration averaged 30.2 ± 5.9 and 420.3 ± 50.5 mg/L, respectively, implying that 390.1 mg/L sulfate was generated. The complete denitrification of 50 mg/L NO_3–N would theoretically generate 377 mg/L sulfate. Increasing the influent nitrate concentration to 75 mg/L NO_3–N in period 5 (days 75–91) adversely affected the bioreactor performance as the
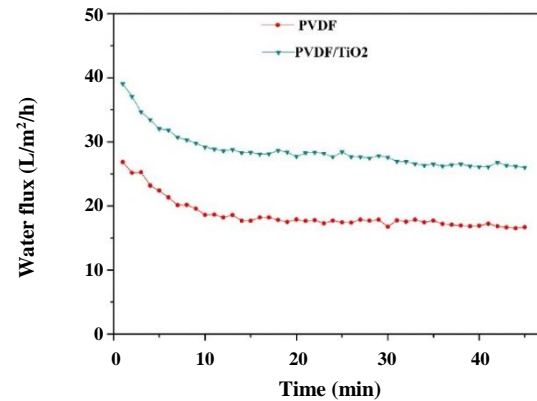
effluent nitrate concentration increased linearly up to around 27.3 mg/L NO_3–N on day 91. Similarly, nitrite was detected at the effluent of the bioreactor in period 5.

In period 6 (days 91–111), the reactor feed was supplemented with higher concentration of methanol. Although the reactor was fed with 75 mg L^{-1} NO_3–N, the effluent nitrate concentration averaged 0.52 ± 0.74 mg/L NO_3–N and nitrite was not detected at the effluent. In the period 7, in order to decrease the effluent sulfate concentration below 250 mg/L, the feed methanol concentration was doubled to 56 mg/L, which decreased the effluent sulfate concentration to 252.2 ± 16.1 mg/L. In period 6, when the influent methanol concentration was 28 mg/L, the alkalinity consumption was 161 mg/L. In period 7, when the bioreactor feed was amended with 56 mg/L, the effluent alkalinity (583.2 ± 97.1 mg/L $CaCO_3$) was slightly higher than the influent value (575.5 mg/L $CaCO_3$), which was due to the increased fraction of nitrate reduced by the heterotrophic denitrifiers. The fraction of heterotrophic denitrification to balance the alkalinity consumption by autotrophic denitrification depends on the type of organic matter used for heterotrophic denitrification. Lee et al.[33] reported that when methanol or acetate was used as a carbon source, complete denitrification without alkalinity addition was observed when 60% and 44%, respectively, of nitrate was denitrified heterotrophically. However, 70% of nitrate should be used by heterotrophs to balance the alkalinity when glucose was used as a carbon source. Decreasing and lastly eliminating the external alkalinity addition (periods 8–10) did not adversely affect the process performance
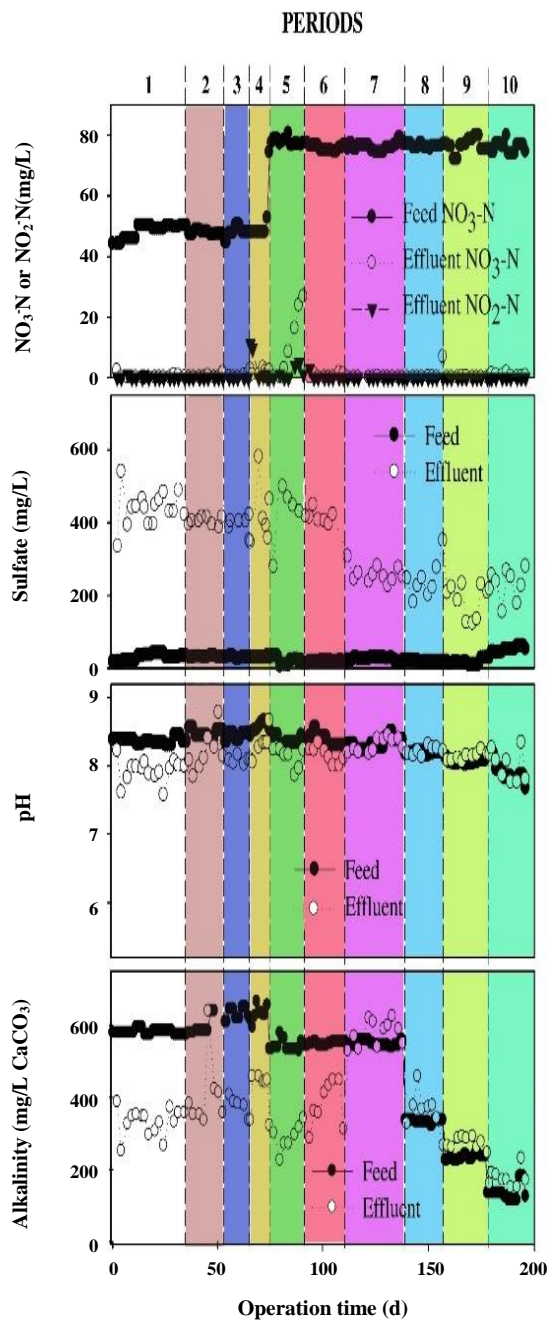
Fig. 12: Feed and effluent NO₃–N, NO₂–N, sulfate, pH, and alkalinity variations.

and the effluent alkalinity values were always slightly higher than the influent ones. Similar to the alkalinity values, the effluent pHs (8.12 ± 0.16) were always equal or higher than the influent values (8.06 ± 0.15). Decreasing or eliminating influent alkalinity did not affect the sulfate

generation as the effluent sulfate concentration after period 7 averaged 220 ± 50 mg/L, which is below the limit value of 250 mg/L. In the study of *Sahinkaya et al.*[34], the maximum autotrophic denitrification efficiency was 0.20 g NO_3^--N/L.d when loading was 0.214 g NO_3^--N/L/d. Similarly, Soares [35] observed the denitrification rate of 0.20 g NO_3^--N/L.d at an HRT of 1.0 h and NO_3^-–N loading of 0.24 g NO_3^--N/L.d. Hence, relatively higher autotrophic denitrification rate was attained in the present study, which may be due to the use of soluble alkalinity source (NaHCO₃) instead of a slowly dissolving one (limestone). Some species of microalgae are enable to shift from autotrophic metabolism to heterotrophic, then, they can benefit from organic and inorganic carbons to supply the source of energy. *Sierra-Alvarez et al.* [36] used denitrifying biofilm granules in sulfur/limestone packed bed reactor and reported the maximum denitrification rate as 0.3 g NO_3^{--}-N/(L d). In our study, the heterotrophic and autotrophic processes were combined in one reactor for nitrate removal from drinking water. This study showed that the combined process in one reactor can completely denitrify 75 mg/L NO_3^-–N even at C:N ratio (mg CH₃OH: mg NO_3^-–N) of 2.0 without external alkalinity supplementation (period 10) and not exceeding the guideline value of 250 mg/L for sulfate. The combined autotrophic and heterotrophic denitrification process can also be used for the denitrification of industrial effluents.

Foglar [37]studied the use of natural zeoliteinteracted with bacterial cells to obtain bio-zeolite particles for nitrate removal, in a continuous-flow stirred reactor. The removal rate of nitrate was 7.97 gNO_3^-/L.d (0.13 mol NO_3^-/L.d) at a hydraulic residence time (HRT) of 1.32 h. *Kesserű* [38] evaluated biological denitrification in a continuous-flow pilot bioreactor containing immobilized *Pseudomonas butanovora* cells. The average removal rates were 3.90 gNO_3^-/L.d (0.004 mol NO_3^-/L.d) and 2.39 gNO_3^-/L.d (0.002 molNO_3^-/L.d) at ethanol–C:nitrate–N ratios of 3:1 and 1.5:1, respectively. *Montalvo* [39] modified an Up-flow Anaerobic Sludge Blanket (UASB) reactor using zeolite to improve the nitrate removal process. The reactor achieved a nitrate removal efficiency of 92.4% and a removal rate of 6.2 gNO_3^-/L.d (0.10 molNO_3^-/L.d) at an HRT of 2.5 h. Isaka [40] evaluated the nitrate removal performance of polyethylene glycol (PEG) gel carriers containing entrapped heterotrophic denitrifying

Table 5: Kinetics coefficients for MPBR.

Parameter	MPBR							
	First-order Model	Second order model				Stover–Kincannon model		
	R^2	k_1	R^2	m	n	R^2	U_{max}	K_s
Nitrate removal	0.56	2.91	0.95	0.89	0.07	0.98	1427.57	1477.53

bacteria in a cylindrical reactor. A maximum nitrate removal rate of 22.58 gNO_3^-/L.d (0.36 $molNO_3^-$/L.d) was observed. Jing [41] studied the performance of an anaerobic reactor for simultaneous sulfide and nitrate removal. The removal rate for nitrate was 4.60 gNO_3^-/L.d (0.07 mol NO_3^-/L.d) at an HRT of 4 h. *Tavares* [42] tested an alternative system, in which anaerobic digestion and denitrification take place in the same UASB. The removal rate was 0.19 gNO_3^-/L.d (0.003 mol NO_3^-/L.d) at an HRT of 6 h. *Barber* [43] carried out the nitrate removal in an anaerobic baffled reactor (ABR). Nitrate removal efficiency was 82% and removal rate was 0.98 g NO_3^-/L.d (0.02 $molNO_3^-$/L.d) with a very high HRT of 20 h. *Cai* [44] proposed using methane in biogas as an electron donor to facilitate complete nitrate removal with Denitrifying Anaerobic Methane Oxidizing (DAMO) microorganisms, in an anaerobic ammonium oxidation (Anammox) reactor. The nitrate removal rate was 3.03 gNO_3^-/L.d (0.05 $molNO_3^-$/L.d) at an HRT of 36 h. *Waki* [45] developed a semi-partitioned reactor to study methane-dependent denitrification. The removal rate was 0.27 gNO_3^-/L.d (0.004 $molNO_3^-$/L.d at an HRT of 72 h. Islas-Lima [46] obtained a high nitrate removal rate of 31.34 gNO_3^- L^{-1} d^{-1} (0.51 $molNO_3^-$/L.d) in a Continuous Stirred Tank Reactor (CSTR). However, the HRT was 48 h.

Kinetics models

To show the relationships among variables for evaluating the results of experiments, kinetics methods are employed. In the present study, the biological kinetics coefficients were analyzed by First- and second-order models as well as the modified Stover–Kincannon model. The average data of performances at experimental runs were used to model the kinetics. Kinetic coefficients of the studied models are shown in Table 4. Based on R^2, modified Stover–Kincannon model was well fitted with the data obtained from nitrate removal in MPBR ($R^2 = 0.98$).

CONCLUSIONS

To our knowledge, this is the first time that a continuous MPBR has been used for nitrate removal from aquatic media. The novel flat sheet PVDF based nanocomposite photocatalytic membrane consisting of TiO_2 nanorods had been successfully prepared via phase inversion method. TiO_2 nanorods were hydrothermally grown and deposited on FTO glass and characterized using XRD, SEM, TEM, SAED and XRD analysis. It is demonstrated that, the deposited TiO_2 thin film shows pure rutile phase with tetragonal crystal structure. The SEM images showed that the nanorods were well-formed on the surface of FTO. TiO_2 hybridized Polyvinylidenefluoride membrane were successfully prepared and characterised by SEM, AFM, FTIR, and the performances of hybrid membrane was determined through the measurements of contact angle, mechanical and thermal properties , porosity distribution, pure water flux and static adsorption toward BSA. The presence of TiO_2 nanofibers in PVDF membrane matrix gave a uniform structure on the entire cross-section of the membrane, which is a porous-like structure. The addition of TiO_2 nanorods into PVDF matrix was found to play an important role in increasing membrane hydrophilicity and enhancing pure water flux. MPBR photobioreactor with solid biofilm carrier was conducted for removal of nitrate from the synthesized wastewater in the laboratory scale. Nitrate reduction using mixotrophic denitrification process showed a good performance (around 99% removal efficiency) when methanol was entered in to the system. The effluent sulfate concentration of the mixotrophic process decreased to the drinking water guideline value of 250 mg/L. Lastly, the proposed process did not require external alkalinity supplementation as the alkalinity need of autotrophic denitrifiers was supplemented by the heterotrophic denitrifiers. These findings suggest that the PMBR water treatment system provided better treatment performance than a conventional MBR.

REFERENCES

[1] Yu X., Jiang Y., Huang H., ShiaKeji J., Zhang W.P., Lv J., Li H., He H., Li X., Simultaneous Aerobic Denitrification and Cr(VI) Reduction by Pseudomonas Brassicacearum LZ-4 In Wastewater, *Bioresource Technology*, **221**: 121-129 (2016).

[2] Satake S., Tang C., Groundwater Nitrate Remediation Using Plant-Chip Bioreactors under Phosphorus-Limited Environment, *Journal of Contaminant Hydrology*, **209**: p. 42-50 (2018).

[3] Darvish M., Moradi Dehaghi S., Taghavi L., Karbassi A.R., Removal of Nitrate Using Synthetic Nano Composite ZnO/Organoclay: Kinetic and Isotherm Studies, *Iran. J. Chem. Chem. Eng. (IJCCE)*, **39(1)**: 105-118 (2020).

[4] Prajapat G., Rellegadla S., AkhilAgrawal S., Reservoir Souring Control Using Benzalkonium Chloride and Nitrate in Bioreactors Simulating Oil Fields of Western Indi, *International Biodeterioration & Biodegradation*, **132**: p. 30-39 (2018).

[5] MoKim Y., Park H., Chandran K., Nitrification Inhibition by Hexavalent Chromium Cr(VI) – Microbial Ecology, Gene Expression and Off-Gas Emissions, *Water Research*, **92**: 254-261 (2016).

[6] Lei Z., Li Y.-y., Wen W., Wang X.C., Chen R., Application of Anaerobic Membrane Bioreactors to Municipal Wastewater Treatment at Ambient Temperature: A Review of Achievements, Challenges, and Perspectives, *Bioresource Technology*, **267**: 756-768 (2018).

[7] Izadi A., Hosseini M., Pajoum Shariati F., Najafpour G., Nabi Bidhendi G., Treatment of Real Paper-Recycling Wastewater in a Novel Hybrid Airlift Membrane Bioreactor (HAMBR) For Simultaneous Removal of Organic Matter And Nutrients, *Iran. J. Chem. Chem. Eng. (IJCCE)*, **38(3)**: 209-220 (2019).

[8] Zhao L., Zhang C., Mutai Bao J.L., Advanced Treatment for Actual Hydrolyzed Polyacrylamide-Containing Wastewater in a Biofilm/Activated Sludge Membrane Bioreactor System: Biodegradation and Interception, *Biochemical Engineering Journal*, **141**: 120-130 (2019).

[9] Nwob E.G., Parlevliet D.A., Laird D.W., Alameh K., Moheimani N.R., Sustainable Phycocyanin Production from Arthrospira Platensis Using Solar-Control Thin Film Coated Photobioreactor, *Biochemical Engineering Journal*, **141**: 232-238 (2019).

[10] Zou X.L., Combination of Ozonation, Activated Carbon, and Biological Aerated Filter for Advanced Treatment of Dyeing Wastewater for Reuse, *Env. Sci. Pol. Res.*, **22(11)**: 8174-8181 (2015).

11. Alsalhy Q.F., Al-Ani F.H., Al-Najar A.E., A New Sponge-GAC-Sponge Membrane Module for Submerged Membrane Bioreactor Use in Hospital Wastewater Treatment, *Biochemical Engineering Journal*, **133**: 130-139 (2018).

[12] Sayadi M., Farasati M., Mahmoodloo M., Rostami F., Removal of Nitrate, Ammonium and Phosphate from Water Using Conocarpus and Paulownia Plant Biochar, *Iran. J. Chem. Chem. Eng. (IJCCE)*, **39(4)**: 205-222 (2020).

[13] Palmarin M.J., Young S., The Effects of Biocarriers on the Mixed Liquor Characteristics, Extracellular Polymeric Substances, and Fouling Rates of a Hybrid Membrane Bioreactor, *Biochemical Engineering Journal*, **141**: 278-284 (2019).

[14] Naghizadeh A., Mahvi A.H., Mesdaghinia A.R., Alimohammadi M., Application of MBR Technology in Municipal Wastewater Treatment, *Arab. J. Sci. Eng.*, **36**(1): 3–10 (2011).

[15] Naghizadeh A., Daraei H.N., Naddafi K., Evaluation of Hollow Fiber Membrane Bioreactor Efficiency for Municipal Wastewater Treatment, *Iran. J. Environ. Health Sci. Eng.*, **5(4)**: 257-268 (2008).

[16] Derakhshan Z., Mahvi A.H., Ehrampoush M.H., Ghaneian M.T., Yousefinejad S., Faramarzian M., Mazloomi S.M., Dehghani M., Fallahzadeh H., Evaluation of Kenaf Fibers as Moving Bed Biofilm Carriers in Algal Membrane Photobioreactor, *Ecotoxicology and Environmental Safety*, **152**: 1-7 (2018).

[17] Foladori P., Petrini S., Andreottola G., Evolution of Real Municipal Wastewater Treatment in Photobioreactors and Microalgae-Bacteria Consortia Using Real-Time Parameters, *Chem. Eng. J.*, **345**: 507-516 (2018).

[18] Zhang X., Wang Y., Liu Y., Xu J., Han Y., Xu X., Preparation, Performances of PVDF/ZnO Hybrid Membranes and their Applications in the Removal of Copper Ions, *Appl. Surf. Sci.*, **316**: 333-340 (2014).

[19] Laera G., Chong M.N., Jin B., Lopez A., An integrated MBR-TiO₂ Photocatalysis Process for the Removal of Carbamazepine from Simulated Pharmaceutical Industrial Effluent, *Bioresource Technology*, **102(13)**: 7012-7015 (2011).

[20] Qin L., Zhang Y., Xu Z., Zhang G., Advanced Membrane Bioreactors Systems: New Materials and Hybrid Process Design, *Bioresource Technology,* **269**: 476-488 (2018).

[21] Naghizadeh A., Shahabi H., F.Ghasemi, Zarei A., Synthesis of Walnut Shell Modified with Titanium Dioxide and Zinc Oxide Nanoparticles for Efficient Removal of Humic Acid from Aqueous Solutions., *J. Water. Health.* , **14**(6): p. 989-997 (2016).

[22] Guldhe A., Kumari S., Ramanna L., Ramsundar P., Singh P., Rawat I., Bux F., Prospects, Recent Advancements and Challenges of Different Wastewater Streams for Microalgal Cultivation, J*ournal of Environmental Management*, **203**: 299-315 (2017).

[23] Ramandi S., Entezari M.H., Ghows N., Solar Photocatalytic Degradation of Diclofenac by N-Doped TiO_2 Nanoparticles Synthesized by Ultrasound, *Iran. J. Chem. Chem. Eng. (IJCCE)*, **39(3)**: 50-173 (2020).

[24] Huang H., Hou X., Xiao J., Zhao L., Li Y., Effect of Annealing Atmosphere on the Performance of TiO_2 Nanorod Arrays in Photoelectrochemical Water Splitting, *Catalysis Today*, **330**: 189-194 (2019).

[25] Zatloukalová K., Obalová L., Kočí K., Čapek L., Matěj Z., Šnajdhaufová H., Ryczkowski J., Słowik G., Photocatalytic Degradation of Endocrine Disruptor Compounds in Water over Immobilized TiO_2 Photocatalysts, *Iran. J. Chem. Chem. Eng. (IJCCE),* **36(2)**: 29-38 (2017).

[26] Bahramian A.R., Enhanced Photocatalytic Activity of Sol-Gel Derived Coral-like TiO_2 Nanostructured Thin Film, *Iran. J. Chem. Chem. Eng. (IJCCE),* **35(2)**: 27-41 (2016).

[27] Zhang J., Wang Z., Liu M., Zhao F., Wu Z., In-Situ Modification of PVDF Membrane During Phase-Inversion Process Using Carbon Nanosphere Sol as Coagulation Bath for Enhancing Anti-Fouling Ability, *Journal of Membrane Science,* **526**: 272-280 (2017).

[28] Li Y., Sun J., Liu L., Yang F., A Composite Cathode Membrane with CoFe2O4–rGO/PVDF on Carbon Fiber Cloth: Synthesis and Performance in a Photocatalysis-Assisted MFC-MBR System, *Environmental Science: Nano*, **4(2)**: 335-345 (2017).

[29] Zhao C., Xu X., Chen J., Wang G., Yang F., Highly Effective Antifouling Performance of PVDF/Graphene Oxide Composite Membrane in Membrane Bioreactor (MBR) System, *Desalination*, **340(1)**: 59-66 (2014).

[30] Song H., Shao J., He Y., Liu B., Zhong X., Natural Organic Matter Removal and Flux Decline with PEG-TiO_2-doped PVDF Membranes By Integration of Ultrafiltration with Photocatalysis, *Journal of Membrane Science*, **405-406**: 48-56 (2012).

[31] Li J.H., Shao X.S., Zhou Q., Li M.Z., Zhang Q.Q., The Double Effects of Silver Nanoparticles on the PVDF Membrane: Surface Hydrophilicity and Antifouling Performance, *Appl Surf Sci*, **265**: 663-670 (2013).

[32] Yu H., Qu F., Zhang X., Wang P., Li G., Liang H., Effect of Quorum Quenching on Biofouling and Ammonia Removal in Membrane Bioreactor under Stressful Conditions, *Chemosphere*, **199**: 114-121 (2018).

[33] Lee D.U., Lee I.S., Choi Y.D., Bae J.H., Effects of External Carbon Source and Empty Bed Contact Time on Simultaneous Heterotrophic and Sulfur-Utilizing Autotrophic Denitrification, *Process Biochemistry,* **36(12)**: 1215-1224 (2001).

[34] Sahinkaya E., Dursun N., Kilic A., Demirel S., Uyanik S., Cinar O., Simultaneous Heterotrophic and Sulfur-Oxidizing Autotrophic Denitrification Process for Drinking Water Treatment: Control of Sulfate Production, *Water Research*, **45(20)**: 6661-6667 (2011).

[35] Soares M.I.M., Denitrification of Groundwater with Elemental Sulfur, *Water Research*, **36(5)**: 1392-1395 (2002).

[36] Sierra-Alvarez R., Karri S., Freeman S., Field J.A., Biological Treatment of Heavy Metals in Acid Mine Drainage Using Sulfate Reducing Bioreactors, *Water Sci. Technol.,* **54(2)**: 179-185 (2006).

[37] Foglar L., Briški F., Sipos L., Vuković M., High Nitrate Removal from Synthetic Wastewater with the Mixed Bacterial Culture, *Bioresource Technology*, **96(8)**: 879-888 (2005).

[38] Kesserü P., Kiss I., Bihari Z., Polyák B., Biological Denitrification in a Continuous-Flow Pilot Bioreactor Containing Immobilized Pseudomonas Butanovora Cells, *Bioresource Technology*, **87(1)**: 75-80 (2003).

[39] Montalvo S., Guerrero L., Robles M., Mery C., Huiliñir C., Borja R., Start-up and Performance of UASB Reactors Using Zeolite for Improvement of Nitrate Removal Process, E*cological Engineering*, **70**: 437-445 (2014).

[40] Isaka K., Kimura Y., Osaka T., Tsuneda S., High-Rate Denitrification Using Polyethylene Glycol Gel Carriers Entrapping Heterotrophic Denitrifying Bacteria, *Water Research*, **46(16)**: 4941-4948 (2012).

[41] Jing C., Ping Z., Mahmood Q., Simultaneous Sulfide and Nitrate Removal in Anaerobic Reactor under Shock Loading, *Bioresource Technology,* **100(12)**: 3010-3014 (2009).

[42] Darvish M., Moradi Dehaghi S., Taghavi L., Karbassi A.R., Removal of Nitrate Using Synthetic Nano Composite ZnO/Organoclay: Kinetic and Isotherm Studies, *Iran. J. Chem. Chem. Eng. (IJCCE)*, **39(1)**: 105-118 (2020).

[43] Barber W.P., Stuckey D.C., Nitrogen Removal in a Modified Anaerobic Baffled Reactor (ABR): 1, Denitrification, *Water Research*, **34(9)**: 2413-2422 (2000).

[44] Cai C., Hu S., Guo J., Shi Y., Xie G.J., Yuan Z., Nitrate Reduction by Denitrifying Anaerobic Methane Oxidizing Microorganisms Can Reach a Practically Useful Rate, *Water Research*, **87**: 211-217 (2015).

[45] Waki M., Suzuki K., Osada T., Tanaka Y., Methane-Dependent Denitrification by a Semi-Partitioned Reactor Supplied Separately with Methane and Oxygen, *Bioresource Technology,* **96(8)**: 921-927 (2005).

[46] Islas-Lima S., Thalasso F., Gómez-Hernandez J., Evidence of Anoxic Methane Oxidation Coupled to Denitrification, *Water Research,* **38(1)**: 13-16 (2004).